

UPCommons

Portal del coneixement obert de la UPC

<http://upcommons.upc.edu/e-prints>

Aquesta és una còpia de la versió *author's final draft* d'un article publicat a la revista [Journal of physics D. Applied physics].

URL d'aquest document a UPCommons E-prints:
<http://hdl.handle.net/2117/91314>

Article publicat¹ / *Published paper*:

Roa, J.J., Coll, A., Bermejo, S., Jiménez-Piqué, E., Alcubilla, R., Castañer, L., and Llanes, L. (2016) Mechanical properties of Al₂O₃ inverse opals by means of nanoindentation. Journal of physics D. Applied physics (49), 45, 455303/1-455303/7
Doi: 10.1088/0022-3727/49/45/455303

Mechanical properties of Al₂O₃ inverse opals by means of nanoindentation

J.J.Roa^{1,2,*}, A.Coll^{2,3}, S. Bermejo³, E.Jiménez-Piqué^{1,2}, R. Alcubilla^{2,3}, L. Castañer³, L. Llanes^{1,2}

¹ CIEFMA – Materials Science and Metallurgical Engineering Department, EEBE-Barcelona East School of Engineering, Universitat Politècnica de Catalunya, 08019 Barcelona, Spain

² Centre for Research in NanoEngineering, EEBE-Barcelona East School of Engineering, Universitat Politècnica de Catalunya, 08019Universitat Politècnica de Catalunya, 08028 Barcelona, Spain

³ MNT, Electronic Engineering Department, Universitat Politècnica de Catalunya, 08034 Barcelona, Spain

* Corresponding author, e-mail: joan.josep.roa@upc.edu

Abstract

In order to understand the mechanical behaviour of Al₂O₃ inverse opals, nanoindentation techniques have been implemented in material layers with three different microstructures, in terms of hollow or polystyrene spheres, with Al₂O₃ shells of distinct wall thickness. Different indenter tip geometries as well as contact loading conditions have been used, in order to induce different stress field and fracture events to the layers. Field emission scanning electron microscopy and focused ion beam have been employed to understand accommodation of plastic deformation induced during the indentation process. Results show that materials with polystyrene spheres exhibit higher hardness and modulus under sharp indentation, and cracking resistance under spherical indentation. Furthermore, deformation is discerned to be mainly governed by the rotation of the microspheres. In the case of the inverse opals made of hollow spheres, the main deformation mechanisms activated under indentation are the rearrangement and densification of them.

Keywords: Al₂O₃ inverse opal, hardness, elastic modulus, stress-strain curve, fracture events, densification

1. Introduction

Inverse opal materials are gaining interest as photonic crystals [1], catalytic supports, capacitors [2], and photocatalytic devices [3], among others. Although it is possible to fabricate inverse opals by lithographic or ion beam techniques [4], self-assembly process is more flexible and cost effective for production [5,6,7]. Conventional self-assembly technologies have achieved either large area layers or highly ordered layers, but hardly both of them [8]. Recently a new technique has been developed enabling to simultaneously produce large area colloidal crystals while keeping good optical quality. This technology, named Electrospray Colloidal Crystal (ECC) deposition [9,10,11], produces centimeter size samples with up to 50 layers of polystyrene or silicon dioxide nanospheres with diameter in the range from 200 nm to 1 µm. The nanoparticle colloidal solution of distilled water is pumped through a small needle of 150 µm in diameter. Then the needle is polarized from -4 kV to -7 kV, and at the same time the

sample is polarized with a high negative voltage, typically between -500 to -1000 V. This technique creates a fine aerosol of charged droplets that, as they reach the surface, induce an ordered deposit of the nanoparticles, due to electrokinetic and drag forces produced by the meniscus of the water while drying. Combining this technique with atomic layer deposition (ALD), it has been shown that inverse opals can be created by filling the inner voids of the ordered nanoparticles ending up in the inverse geometry of a colloidal crystal [2].

Although it has been shown that these structures exhibit good thermal stability [2], there is not any knowledge on the mechanical properties of these layers. This work is aimed to analyze the micromechanical response of alumina inverse opals [4,8]. Although the mechanical response of silica colloidal crystals [5], capped nanocrystals and supercrystals films [6,7,12], and polymer-stabilized or sintered aggregates [13], has been studied by nanoindentation at the nanometric length scale; similar information at the micrometric length scale of Al_2O_3 inverse opals is not available in the open literature. In this study, nanoindentation techniques are used for reliable micromechanical characterization of Al_2O_3 inverse opal under different contact stresses, mainly to determine the elastic and elasto-to-plastic properties.

2. Experimental procedure

Colloidal crystal electrospraying [9] was used to produce the layers used in this work. The silicon substrate was contacted to a high voltage power supply (Ultravolt high-voltage bipolar source, -15 kV to +15 kV, Ronkonkoma, NY, USA.) through a patterned electrode of aluminum or ITO (Indium tin oxide) at -500 to -1000 V. On the other side, a needle at 2.5 cm distance was contacted at 6 kV. Through the needle an off-the-shelf nanofluid, composed of distilled water and 260 nm polystyrene nanoparticles diameter at a concentration of 25 mg/ml, was dispensed. This nanofluid was pumped by an infusion pump (B. Braun SA, Melsungen, Germany). Colloidal crystals with up to 50 layers with ordered spheres in close packed disposition were created.

Once the colloidal crystal was formed, samples were introduced in an atomic layer deposition (ALD) reactor, where a layer of Al_2O_3 was conformally deposited with a thickness of either 10 nm or 20 nm. Hollow spheres were then created by burning the polymer in an oven at 450 °C for 2 hours (heating curve of 5°C/min).

Three different inverse opal materials were fabricated which were made of: 1) Hollow spheres with 10 nm thick Al_2O_3 shell (labelled as H10); 2) Hollow spheres with 20 nm thick Al_2O_3 shell (labelled as H20); and 3) Polystyrene spheres with 20 nm thick Al_2O_3 shell (labelled as P20), identical to H20, but without the polymer burning step, see

Figure 1.

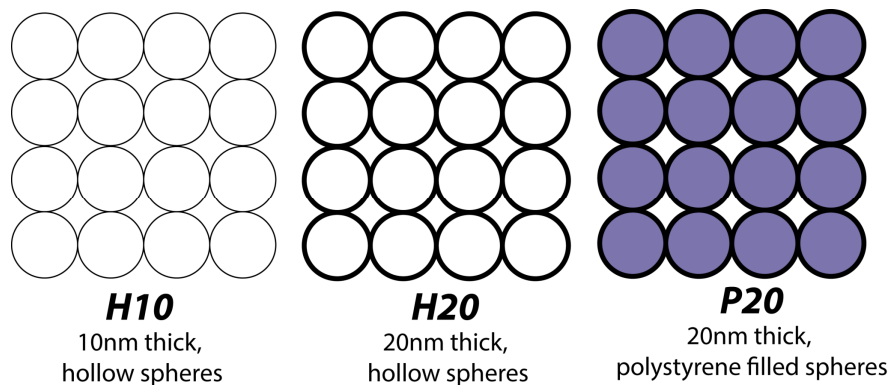


Figure 1. Sketches for the inverse opal microstructures investigated here.

Materials were mechanically tested with a Nanoindenter XP from MTS using blunt and sharp indenter tips. For blunt indentation, diamond spherical tip of 25 μm radius was used, and experimental data were treated using Hertzian equations [14,15,16,17,18,19]. For sharp indentation, the materials were indented with a Berkovich tip, and experimental data were analyzed using the Oliver and Pharr method [20,21]. The Berkovich indenter shape was calibrated with a fused silica standard [20]. A homogeneous indentation array of 16 imprints (4 by 4) were done for each indenter tip at 1000 nm of maximum penetration depth. Loading/unloading as well as peak hold times were selected to be constant for all imprints, 30 and 10 s, respectively. The distance between imprints was 50 μm .

Sub-surface damage was inspected by focused ion beam/field emission scanning electron microscopy (FIB/FESEM) using a Zeiss Neon 40 system. A thin platinum layer was deposited on the sample prior to milling with the aim of reducing ion-beam damage. A Ga^+ ion source was used to mill the surface at a voltage of 30 kV. The final polishing of the cross-section was performed at a current of 500 pA and 30 kV acceleration voltage.

3. Results and Discussion

3.1. Sharp indentation: hardness and elastic modulus

Variation in hardness and elastic modulus as a function of the penetration depth is shown in **Figures 2a** and **b**. Such data was attained by implementing the continuous stiffness measurement option. Data variation and scatter observed at low indentation depths is a direct consequence of surface topography (and possibly indenter tip defects too). Thus, it may be described as a length scale effect (rather than a size one) on indentation response. On the other hand, for the load range studied, hardness and elastic modulus data becomes stable for penetrations deeper than 200 nm, i.e. at about 20 times the corresponding topography length scale in the materials here studied. Values of hardness and elastic modulus gathered within the referred stable regime are summarized in **Table 1**. Hardness and elastic modulus (**Figure 2**) reveals that these properties increase as the sphere diameter increases, being the filled specimen the hardest and the stiffest one.

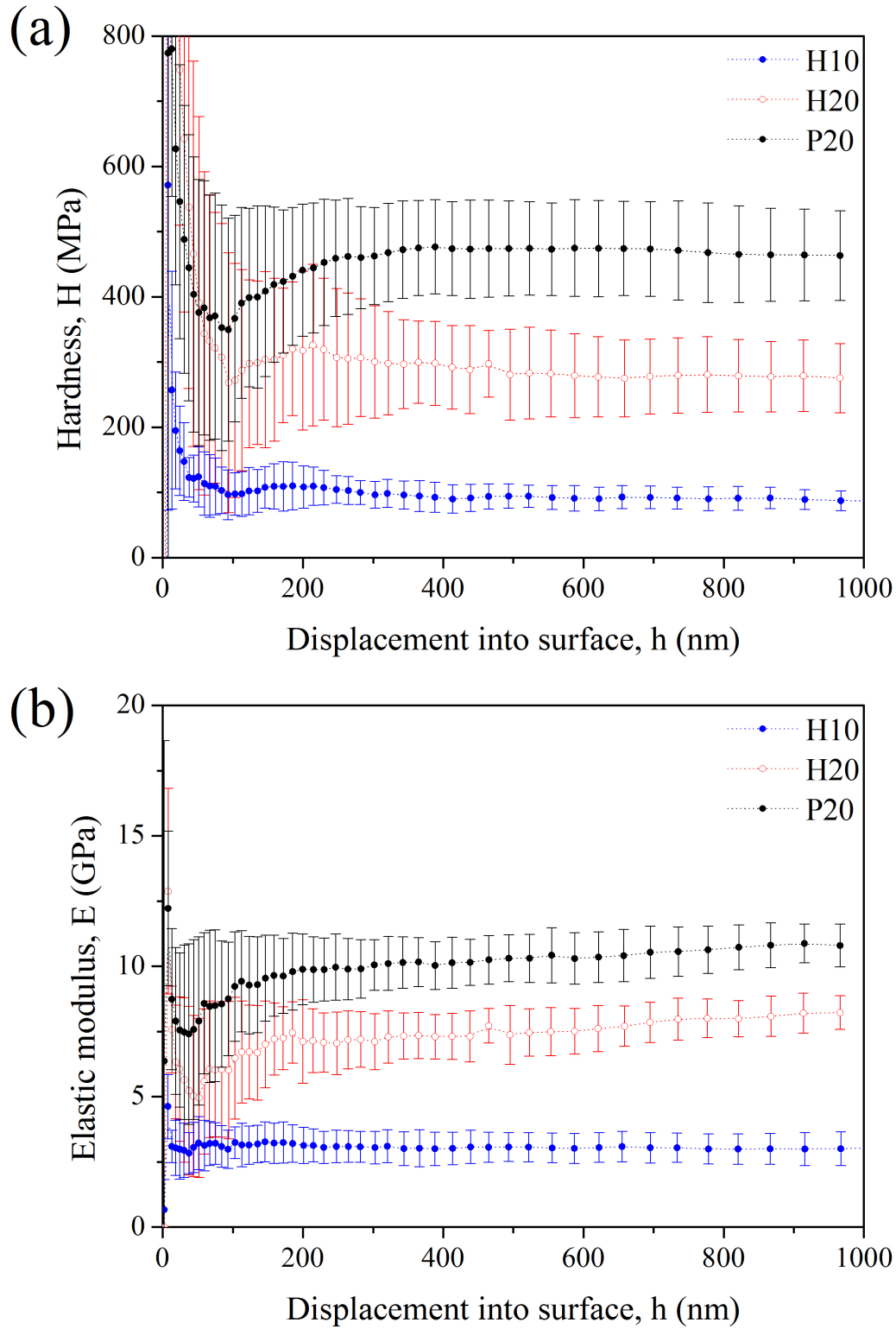


Figure 2. Mechanical properties as a function of the displacement into surface. (a) Hardness, and (b) elastic modulus.

These values are higher than that of the silica colloidal crystals reported by Gallego-Gómez *et al.* [5Error! No s'ha definit el marcador.] and by Wang *et al.* [22]. A possible reason for it is the fact that the materials here studied show strong physical connection linkages among the spheres. Similar comments may be done regarding the

elastic modulus trend observed in **Figure 2b**, on the basis of results directly extracted by simultaneous nanoindentation and 3D imaging on semicrystalline colloidal films reported by Roth and co-authors [23] (i.e. elastic modulus of 1.72 ± 0.27 GPa).

Table 1. Hardness and elastic modulus for the different specimens investigated at maximum penetration depth.

Specimen	Hardness, H (MPa)	Elastic modulus, E (GPa)
H10	87 ± 13	3.0 ± 0.7
H20	275 ± 53	8.2 ± 0.6
P20	463 ± 69	10.8 ± 0.8

3.2. Blunt indentation: **indentation** stress-strain curves

Typical indentation load-displacement curves obtained with the 25 μm indenter at 100 and 500 nm of maximum displacement into surface for the H20 specimen are presented in **Figure 3**. The response for the maximum penetration depth of 100 nm was elastic. The loading curve for the maximum displacement into surface of 500 nm presents a pop-in at a penetration depth of around 230 nm. At this depth, the elasto-plastic transition takes place.

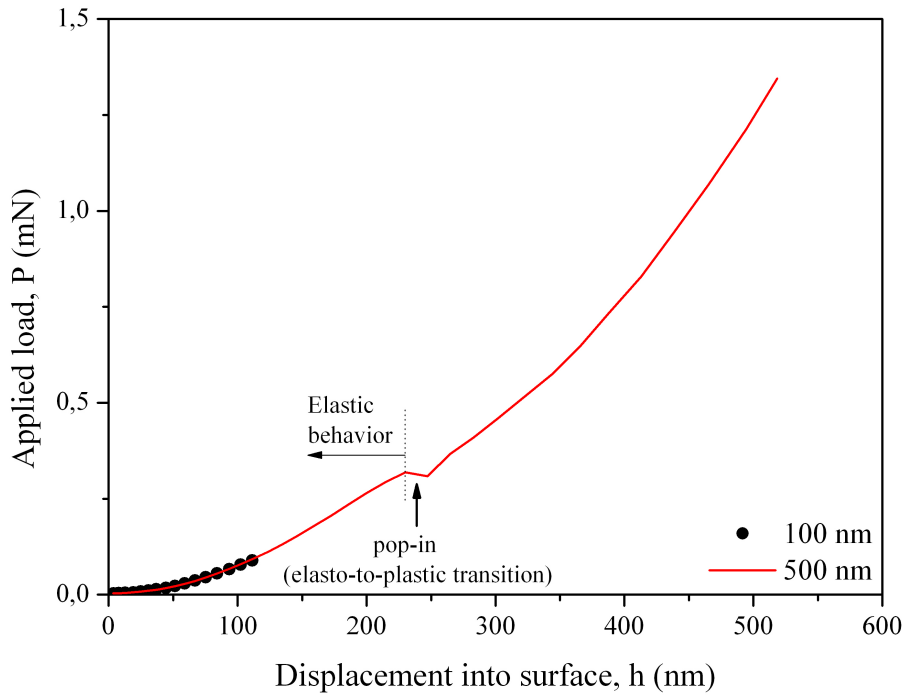


Figure 3. Characteristic loading curves at 100 (elastic response) and 500 nm (elasto-plastic response) of maximum penetration depth for the H20 specimen. Similar trends (not represented here) were discerned for the H10 and P20 materials.

Figure 4 presents the indentation stress against the indentation strain for the different materials, as calculated from the load-displacement experimental curve. As it can be appreciated, three apparent regions (initial contact, elastic and inelastic) may be discerned in the curve. The first region of the curve is produced during the initial contact of the indenter with the surface, and is due to the existence of a non-flat surface. After that, the curve is elastic and the stress is transferred through the walls of the

spheres. Once a critical stress is reached (19.2 MPa in the case of the H10 material), inelastic deformation emerges. These three regions are also appreciated for the H20 and P20 materials. Main differences among the indentation stress-strain plots are found in the inelastic region. For the H10 sample, several pop-in events can clearly be appreciated (labelled as * in **Figure 4**). They are related to fracture and collapse of the material. On the other hand, P20 specimen exhibits higher resistance to deformation, with no discontinuities visible in the indentation stress-strain curve. This resistance can be simply attributed to the fact that the Al_2O_3 spheres are filled with polymer. Mean contact stress and strain values, for which deviation from the elastic regime occurred, are listed in **Table 2**.

The indentation stress-strain curve for P20 material is represented in **Figure 4**. For this coating, the elasto-to-plastic transition takes place at indentation strain of about 10 %. In this case, the indentation stress-strain in the inelastic region increased gradually. This effect is due to the role played by the polymer in accommodating the plastic field induced during indentation.

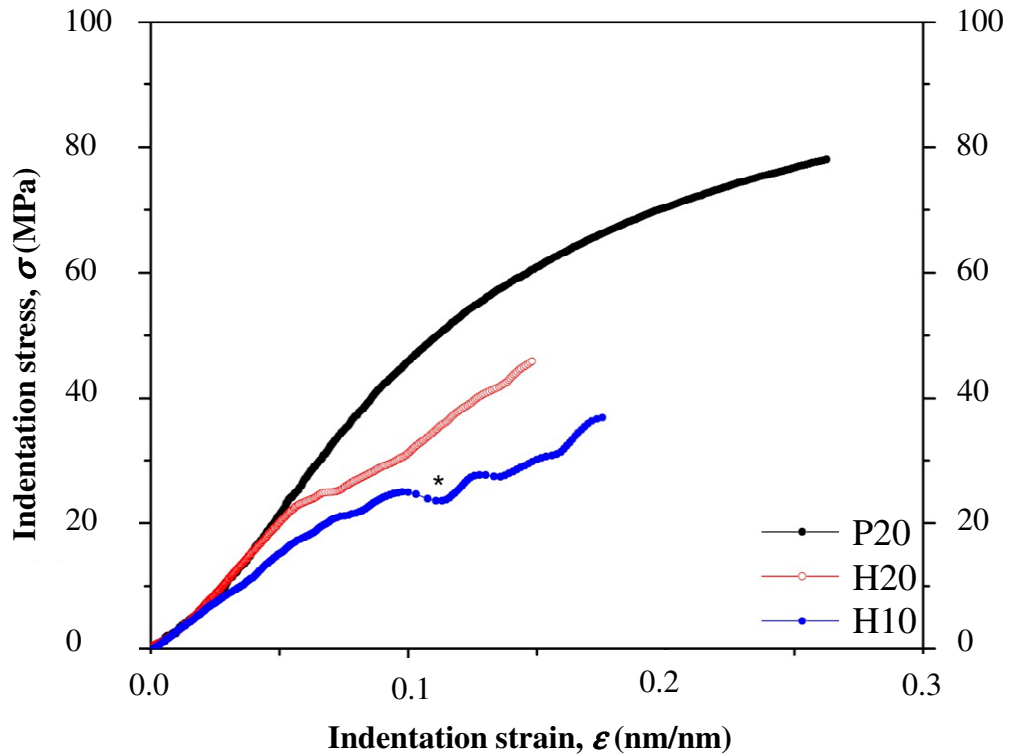


Figure 4. Indentation stress-strain curve for the Al_2O_3 inverse opal specimens: H10, H20, and P20.

Table 2. Main parameters directly extracted from the indentation stress-strain curves.

Specimen	Mean contact pressure, p_m (MPa)	Strain _{elasto-plastic} , ϵ (%)
<i>H10</i>	$5.6. \pm 0.3$	≈ 2
<i>H20</i>	19.2 ± 0.5	≈ 5

<i>P20</i>	45.6 ± 0.6	≈ 10
------------	----------------	--------------

3.3. Deformation and densification mechanisms

Figures 5a and **b** present FESEM images of the Berkovich tip residual imprints. A general view of the residual imprint is shown on the left hand side, whereas a close-up one, highlighting main fracture mechanism, is presented on the right hand side. The surrounding region of the indentation presents a heterogeneous microstructure of pre-existing defects created during the sintering process of these specimens; i.e. cracks ranging between several nanometers up to the micrometer level, porosity, and even in some regions a misorientation of the different spheres. These superficial heterogeneities contribute to increase the scattering of the recorded data during the firsts stages of indentation (≈ 200 nm) in the hardness and elastic modulus data presented in **Figure 2**. Moreover, it is possible to appreciate that residual imprints for both H10 and H20 materials, exhibit low density of microcracks surrounding the residual imprint. Regarding deformation and fracture mechanisms under sharp indentation both hollow specimens show similar behaviour: collapsing and densification of the Al_2O_3 spheres.

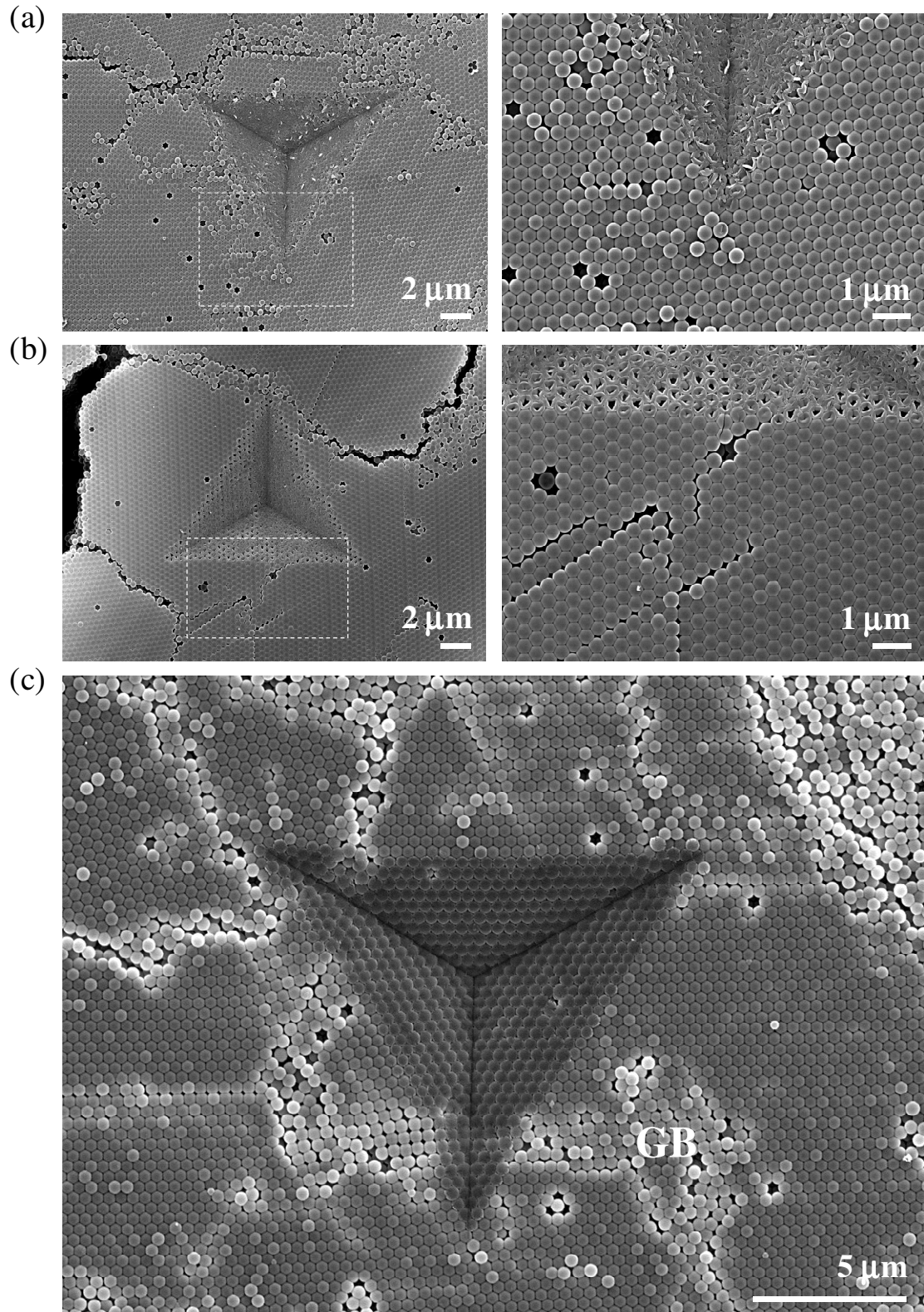


Figure 5. FESEM images of a Berkovich imprint surface at 1000 nm of maximum penetration depth for the different specimens investigated: (a) H10, (b) H20, and (c) P20. The white dash square represents the FESEM magnification for the specimens with hollow spheres (just in one side of the residual imprint), and GB in (c) denotes the grain boundary, *between different orientation domains*.

Figure 5c shows the residual imprint for the P20 sample. In this micrograph it is possible to appreciate that this specimen presents less density of both superficial defects created during the pyrolysis process and damage events surrounding the area of interest. In this particular case, the plastic field induced by the indenter is absorbed and accommodated by the polymer. Furthermore, no cracking or densification is appreciated. In this situation, the plastic field induced during indentation produces a deformation of the spheres.

Attempting to get a more detailed view of the referred damage scenario, FIB cross-sectional images of the residual indentation imprint were conducted, as shown in **Figure 6**. No cracks are appreciated as a consequence of the indentation process. However, a small volume of densification for the collapsed spheres, with a depth of around 500 nm is observed just under the residual imprint for both specimens. Furthermore, below the elasto-plastic region, the Al_2O_3 spheres are intact. Similar finding was reported by Ng and co-workers for anodic aluminium oxide nano-honeycombs [24,25,26]. On the other hand, for the P20 sample, the Al_2O_3 spheres do not collapse, but rather deform producing a partially shearing of the microspheres due to the shear stresses produced by the indentation (maximum just under the central part of the residual imprint).

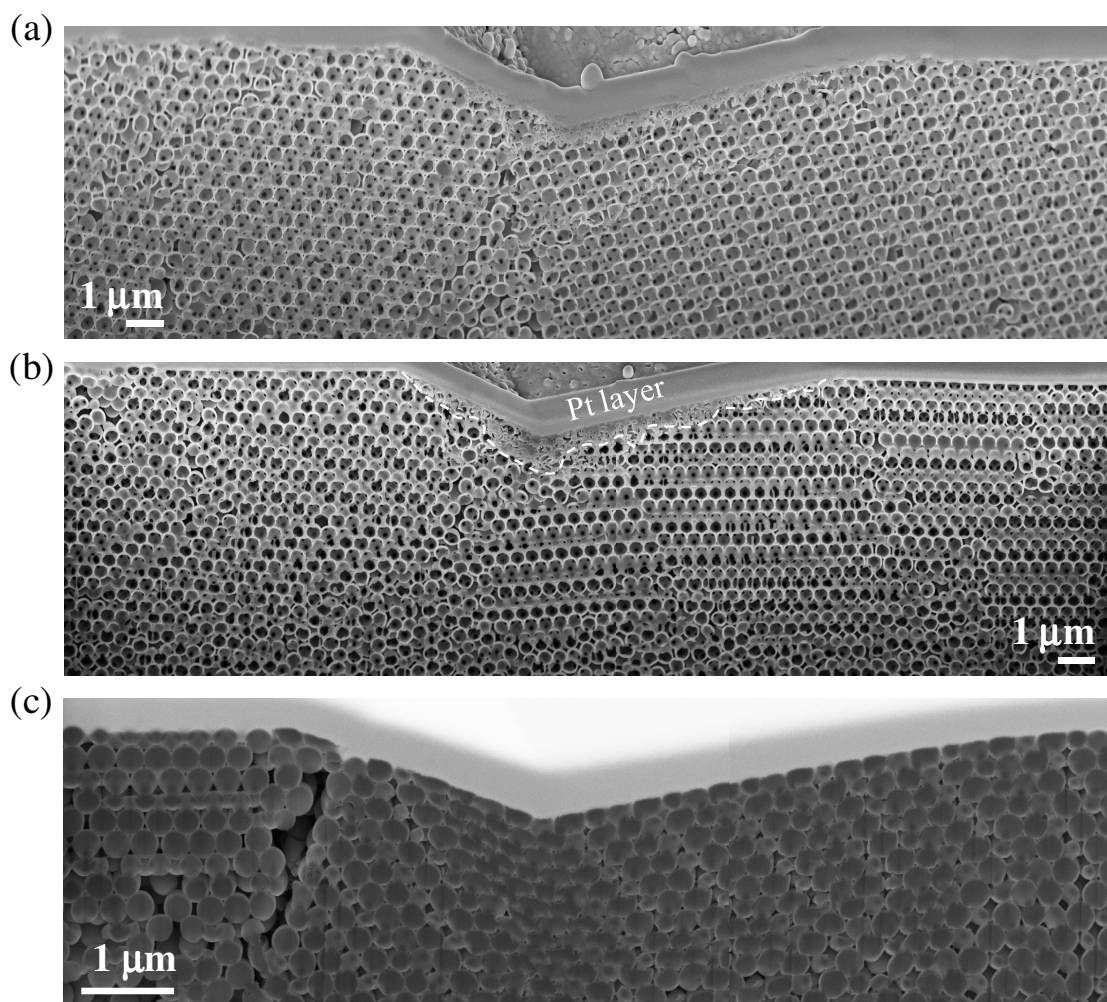


Figure 6. Cross-sectioning and imaging of damage under Berkovich indentation using the FIB/FESEM. (a) H10, (b) H20, and (c) P20. The white dash line presents in (b) denotes the accumulated deformation in terms of collapse produced during the indentation process.

3.4. Elastic modulus vs. porosity

The elastic properties depend on the total porosity, resulting in a reduction of this mechanical parameter when the porosity increases [27,28]. Luo and Stevens [29] reported an empirical equation which relates the elastic modulus to the porosity shape, as follows:

$$E = E_0 \frac{1 - P}{1 + \alpha P} \quad (1)$$

where E_0 corresponds to the elastic modulus of a pore-free material (375 GPa [30]), P is the porosity volume fraction and α is a parameter which is related to the shape of the pores. For spherical pores α has a value of 1, and it decreases to 0.1 for a spheroid shape [29].

Figure 7 presents the experimental values obtained for the measurements of the two elastic moduli for the non-filled specimens (H10 and H20) investigated here by means of sharp indentation. The elastic moduli were fitted using equation 1, taking an α value of 1 for spherical pores. H10 and H20 fraction porosities are 0.99 and 0.975, respectively, see **Figure 6a** and **6b**. Data for P20 is not presented in this graph due to its filled-like character. Consideration of this material would require recalling some viscoelastic models to correctly determine the real elastic modulus, and it is out of the scope of this study.

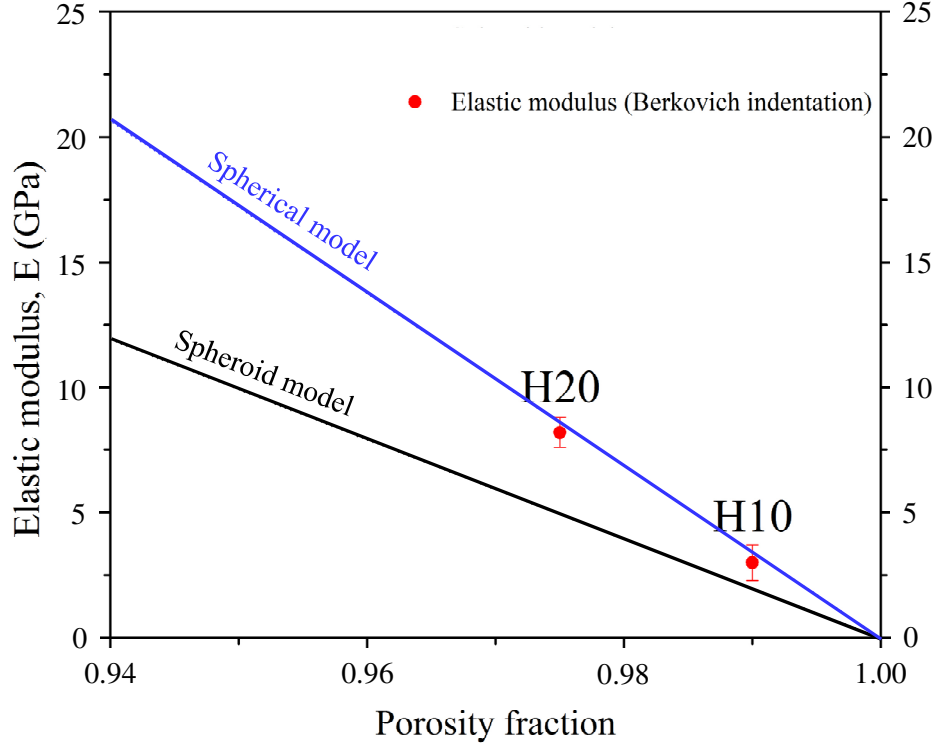


Figure 7. Effect of porosity fraction for specimens on elastic modulus determined by sharp indentation.

4. Conclusions

In this study the mechanical properties (indentation stress-strain curve, elastic modulus and hardness) of Al_2O_3 inverse opals have been characterized by means of nanoindentation testing using different tip geometries. The surface and sub-surface fracture mechanisms have been studied by FESEM and FIB techniques. The following conclusions may be drawn:

- The elastic-to-plastic transition occurred at mean contact pressure ranging from 5.6 up to 45.6 MPa being cracks, the predominant fracture mechanisms for the hollow specimens.
- Hardness and elastic modulus increase as the sphere diameter increases, being the filled specimen the hardest and the stiffest one. Regarding deformation and fracture mechanisms under sharp indentation, both hollow specimens shown similar behaviour: collapse and densification of the Al_2O_3 spheres. However, for the filled specimen no cracking or densification is appreciated. In this situation, the plastic field induced during indentation produces a deformation of the spheres.
- The elastic modulus has a significant influence on the bulk modulus of materials. The spherical model proposed by Luo and Stevens [29] can be fitted to the experimental results for the hollow specimens. **It points out microstructural defects (i.e. porosity) have a strong influence on the elastic field response.**

Acknowledgements

We are grateful to “*Direcció General de Recerca del Comissionat per a Universitats i Recerca de la Generalitat de Catalunya*” for recognizing CIEFMA as consolidated Research Group (2014SGR). This work has been partially supported by the Spanish Ministry of Science and Innovation under projects TEC2011-26329 and the Network of Excellence ‘Nanophotonics for Energy’ GA 248855. Dr. J. J. Roa would like to thank the Juan de la Cierva Programme for its financial support (grant number: JCI-2012-14454). This work has been partially supported by project MAT2015-70780-C4-3-P, AYA-2011-29967-C05-04 and ESP2014-54256-C4-2-R

References

-
- [1] Zhang H G, Yu X D and Braun P V 2011 *Nature Nano.* **6** 277.
 - [2] Coll A, Bermejo S, Martin I and Alcubilla R 2015 *Micro. Eng.* **145** 29.
 - [3] Waterhouse G I N, Wahab A K, Al-Oufi M, Jovic V, Anjum D H, Sun-Waterhouse D, Llorca J and Idriss H 2013 *Scien. Report.* **3** 1.
 - [4] Zhao Y, Xie Z, Gu H, Zhu C and Gu Z 2012 *Chem. Soc Rev.* **41** 3297.
 - [5] Gallego-Gómez F, Morales-Flórez V, Blanco A, Rosa-Fox N de la and López C 2012 *Nano Letters.* **12** 4920.
 - [6] Klajn R, Bishop J M B, Fialkowski M, Paszewski M, Campbell C J, Gray T P and Grybowski B A 2007 *Science.* **316** 261.
 - [7] Lee D, Jia S, Banerjee S, Bevk J, Herman I P and Kysar J W 2007 *Phys. Rev. Lett.* **98** 026103.
 - [8] Galisteo-López J F, Ibisate M, Sapienza R, Froufe-Perez L, Blanco A and Lopez C 2011 *Adv. Mater.* **23** 30.
 - [9] Coll A, Bermejo S, Hernández D and Castañer L 2013 *Nanoscale Res. Lett.* **8** 2.
 - [10] Coll A, Bermejo S and Castañer L 2014 *Microelectron. Eng.* **121** 68.

-
- [11] Castañer L, Bermejo S and Coll A (UPC) Spain. “Procedimiento para el depósito ordenado de capas de metamateriales a partir de soluciones coloidales de micro o nano esferas”, WO 2013001128 A1, (2013).
- [12] Tam E, Podsiadlo P, Schevchenko E, Ogletree D F, Delplancke-Ogletree M P and Ashby P D 2010 *Nano Lett.* **10** 2363.
- [13] Yaghoubi H, Taghavinia N, Alamdari E K and Volinsky A A 2010 *ACS Appl. Mater. Interfaces* **2** 2629.
- [14] Field J S and Swain M V 1993 *J. Mater. Res.* **8** 297.
- [15] Field J S and Swain M V 1995 *J. Mater. Res.* **10** 101.
- [16] Moseson A J, Basu S and Barsoum M W 2008 *J. Mater. Res.* **23** 204.
- [17] Jiménez-Piqué E, Gaillard Y and Anglada M 2007 *Key Eng. Mater.* **333** 107.
- [18] Basu S, Moseson A and Barsoum M W 2006 *J. Mater. Res.* **21** 2628.
- [19] Roa J J, Jiménez-Piqué E, Capdevila X G and Segarra M 2010 *J. Eur. Ceram. Soc.* **30** 1477.
- [20] Oliver W C and Pharr G M 1992 *J. Mater. Res.* **7** 1564.
- [21] Oliver W C and Pharr G M 2004 *J. Mater. Res.* **19** 3.
- [22] Wang J, Wen Y, Ge H, Sun Z, Zheng Y, Song Y and Jiang L 2006 *Macromol. Chem. Phys.* **207** 596.
- [23] Roth M, Schilde C, Lellig P, Kwade A and Auernhammer G K 2012 *Chem. Lett.* **41** 1110.
- [24] Ng KY, Lin Y and Ngan AHW 2009 *Acta Mater.* **57** 2710.
- [25] Ng KY, Zuo L and Ngan AHW 2011 *J. Mech. Phys. Solids* **59** 251.
- [26] Ng KY, Lin Y and Ngan AHW 2012 *Scripta Mater.* **66** 439.
- [27] Rice RW. Porosity of ceramics. New York: Marcel Dekker; 1998.
- [28] Chintapalli R K, Jiménez-Piqué E, Marro F G, Yan H, Reece M and Anglada M 2012 *J. Eur. Ceram. Soc.* **32** 123.
- [29] Luo J and Stevens R 1999 *Ceram. Int.* **25** 281.
- [30] Gault C, Platon F and Le Bras D 1985 *Mat. Sci. Eng.* **74** 105.